Modeling the Flow and Transport Dynamics in Gasoline Particulate Filters to Improve Filtration Efficiency

Svyatoslav Korneev[1]
Department of Energy Resources Engineering,
Stanford University,
Stanford, CA 94305
e-mail: skorneev@stanford.edu

Simona Onori[2]
Department of Energy Resources Engineering,
Stanford University,
Stanford, CA 94305
e-mail: sonori@stanford.edu

We propose a new pore-scale/channel model, or hybrid model, for the fluid flow and particulate transport in gasoline particulate filters (GPFs). GPFs are emission control devices aimed at removing particulate out of the exhaust system of a gasoline direct injection engine. In this study, we consider a wall-flow uncoated GPF, which is made of a bundle of inlet and outlet channels separated by porous walls. The particulate-filled exhaust gas flows into the inlet channels, and passes through the porous walls before exiting out of the outlet channels. We model the flow inside the inlet and outlet channels using the incompressible Navier–Stokes equation coupled with the spatially averaged Navier–Stokes equation for the flow inside the porous walls. For the particulate transport, the coupled advection and spatially averaged advection–reaction equations are used, where the reaction term models the particulate accumulation. Using OPENFOAM, we numerically solve the flow and the transport equations and show that the concentration of deposited particles is nonuniformly distributed along the filter length, with an increase of concentration at the back end of the filter as Reynolds number increases. Images from X-ray computed tomography (XCT)-scanning experiments of the soot-loaded filter show that such a nonuniform distribution is consistent with the prediction obtained from the model. Finally, we show how the proposed model can be employed to optimize the filter design to improve filtration efficiency. [DOI: 10.1115/1.4046151]

1 Introduction

Gasoline direct injection (GDI) engines are touted as providing superior performance, in terms of power out and fuel economy, to port fuel injection technology by using a stratified charge as opposed to the conventional homogeneous charge. The heterogeneous charge, though, is responsible for certain diesel-like features leading to particles emitted by GDI engines to be higher than the Euro 6c limit of $6 \times 10^{11} \#/\text{km}$. The higher operating fuel pressure in GDI systems and better atomization of the fuel entering the cylinders allow for higher power out when compared to port fuel injection engines. The problem of fuel wall wetting in the port is avoided in GDI engines as fuel is directly injected into the engine cylinders thus optimizing the mass of fuel with a more precise air–fuel ratio control. As the penetration of GDI engines in the market has seen an exponential growth over the past decade with positive trend predicted in the coming years, concerns reside in the unwanted and hazardous particulates emitted by GDI engines. Fuel droplets not completely evaporated that exit the engine as unburned hydrocarbons due to the direct injection of fuel into the chamber and the shorter air/fuel mixing times are the causes of such an undesired output [1]. Particulate matter is a complex mixture including organic and inorganic particles, such as soot and smoke, that vary in size and composition. Of interest in this paper is the fine particulate matter with a diameter of $2.5\,\mu\text{m}$ (PM$_{2.5}$) or less. Soot particles, which can make up to 20% of fine particles [2] and are regenerated by initiating a carbon oxidation reaction [3,4], are mainly constituted by carbon. The mean diameter of the particles is of the order of $70 - 80\,\text{nm}$ at peak concentration [5]. Several particulate emission mitigation options for

GDI engines are being actively pursued, from the development of new engine control strategies (i.e., multiple-injection strategy) and modification of fuel properties [6,7] to the adoption of emission mitigation devices, such as gasoline particulate filters (GPFs) [8–10]. The adoption of GPFs to meet the new real-world-driving emissions standards to reduce particulates generated by GDI engines is the solution pursued today by all automakers.

Gasoline particulate filters, installed in the tailpipe of GDI operated vehicles, have been synthesized in a variety of shapes ranging from circular to oval cross section [11]. A wall-flow GPF is made of cordierite, a monolithic porous ceramic body with axially parallel channels alternately blocked off by plugs to force the flow across the porous walls and trap soot inside the walls. With a characteristic pore size, l, in the range of $10 - 20\,\mu\text{m}$ and porosity, ϕ, of 0.5 [12], GPFs are similar to diesel particulate filters (DPFs) [13,14]. A cross section of the cylindrical GPF used in this study is shown in Fig. 1.

Over time, the accumulated soot increases the back pressure to the engine, impacting engine performance and fuel economy and
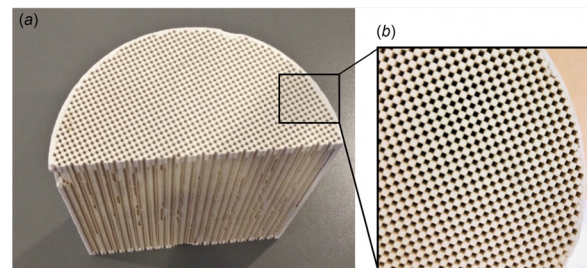

Fig. 1 (a) Cross section of the ceramic monolith used in gasoline particulate filters with the multiple channels of pathways through which both exhaust gas transport and soot particle accumulation occur. (b) Zoom-out of the filter substrate with alternate channels blocked off by plugs.

inducing the permeability of the porous structure to decrease. Regeneration, or oxidation, of soot must be performed periodically to remove the soot trapped in the filter. This can be initiated either passively or actively. Passive regeneration consists in a spontaneous oxidation process during normal driving conditions. To promote the oxidation reactions, a catalytic coating of the porous wall is generally required. The coating material for GPF is similar to those used in three-way catalytic converters [15] and it mainly consists of Ceria and mixture of precious metals. The catalytic coating serves two main functions. First, it decreases the activation energy for the oxidation reaction, so the oxidation happens at lower temperature. Second, it stores/releases the oxygen when the engine operates under a nonstoichiometric condition. The active regeneration, instead, is commanded by the engine control unit by triggering off high oxygen concentration under high temperature conditions in the exhaust system. The active regeneration mechanism is not adopted in today's GPFs.

Despite having the same design, filtration mechanisms in GPF and DPF are different. In DPFs, the filtration mode changes after a saturation load value is reached and a soot cake starts to grow on the porous wall and acting a "plug" toward the back of the channel [16]. Experimental evidence shows that DPF can operate in the so-called deep bed filtration, or cake filtration, regime characterized by a linear dependence of the pressure drop on the accumulated particulate mass in the filter [7]. In GPFs, on the other hand, one can ignore the deep bed filtration regime, as the particle concentration is smaller and the exhaust is hotter, and a cake never develops [17]. Moreover, experimental measurements of particle concentration inside the filter show that the process of the particulate deposition is nonuniform [12,18], in that the particles tend to accumulate predominantly at the back end of the filter. It was also shown that the filter length does not play a crucial role in the filtration efficiency [19]. Here, authors showed that the particulate emission does not change significantly and stays below the target value when varying the GPF length from 5 cm to 12.7 cm. Modeling tools are desirable to understand, analyze, and optimize the performance of the system in light of such an experimental evidence. The knowledge of the flow and the particulate transport dynamics could greatly help to optimize GPF design, for instance, under different flow conditions. As the GPF is the proposed technology to reduce the amount of particulate matter from vehicle exhaust, improvements in the filtration efficiency, active regeneration, and reduction of the pressure drop across the filter call for ad hoc modeling tools to assist the design of real-time estimation and control strategies.

In this paper, we develop a computationally efficient pore-scale/channel, or *hybrid*, model to predict the flow and particulate transport dynamics in GPFs. To the best of our knowledge, this constitutes the first ever proposed physics-based high fidelity model of such a device. The model has the following purposes: (1) to study filtration efficiency, monitor particles deposition, and characterize design properties and flaws and (2) to serve as a modeling platform and benchmark to design lumped-parameter (or reduced-order) models for on-board estimation and control strategies. Such tools will accelerate the advancement of on-board diagnostics and health monitoring methods, particularly relevant for emission testing under real world driving conditions. Preliminary results of the proposed model were first presented by the authors in Ref. [20].

The paper is structured as follows: In Sec. 2, we revise different modeling approaches proposed in the literature for GPF dynamics, and outline the challenges of designing a GPF multiscale dynamical model. In Sec. 3, the *periodic unit* cell is introduced to define the computational domain with the periodic boundary conditions (BCs). In Secs. 4 and 5, the flow and transport equations, as well as their dimensionless formulation, are presented. In Sec. 6, we perform numerical simulations of the flow and the transport equations and show that the concentration of particles inside the porous wall increases with the distance downstream of the flow. In Sec. 7, a CT-scan imaging study performed over uncoated

clean and soot-loaded filters is presented. The CT-scan images are used to extract the longitudinal distribution of the particle inside the filter. Such an information is shown to be consistent with the results obtained from the numerical simulation. In Sec. 8, conclusions of the work presented are summarized and a new simulation study showing how the proposed hybrid model can be used to develop new filter designs to achieve improved filtration efficiency is outlined in future work.

2 Modeling Approach

Although a wealth of literature and experience exist on DPFs, in terms of experimental investigation, available data, and modeling tools, quite little, on the other hand, has been done for GPFs, particularly on physics-based modeling at different scales.

The flow in the wall-flow filter modeled in [21] shows that the suction velocity is nonuniform along the porous wall of the inlet channel and that this effect is more drastic when the flow velocity at the inlet is higher. Reference [22] models the dynamics of soot oxidation in an uncoated GPF using a zero-dimensional model for the thermal and the soot oxidation dynamics, where spatial dependence of the temperature, the flow, and the species concentration were neglected. A zero-dimensional model for a coated GPF was developed in [23], where authors consider the oxygen storage dynamics in addition to the soot oxidation and internal temperature. In Ref. [24], a 2D model of the flow, the thermal, and the chemical dynamics were modeled and experimentally validated for an uncoated GPF.

In Refs. [25] and [26], the authors propose a probability density function-based approach to estimate the filtration efficiency in GPFs. Particles size distribution, flow velocity, and pore-size heterogeneity were treated as stochastic parameters and the filtration efficiency estimated from the probability density function approach was compared with measured data showing good agreement with model predicted results. Despite providing the reasonable estimation of the efficiency, this approach does not explain the nonuniform particles deposition and its relation with the channel geometry. A 1D + 1D single-channel model was proposed in [27] and experimental and simulation studies were performed to investigate the cold start behavior of the filter. Filtration and regeneration mechanisms in GPFs, which continuously oxidize loaded soot, were not clearly understood.

The lack of a thorough understanding of regeneration and accumulation events, is the main reason behind the absence of modeling tools to describe in detail the GPF dynamics. This constitutes the main motivation of this paper. For the very first time, a multiscale (pore-to-continuum) modeling framework is proposed to resolve the mass, energy, and momentum transport of the exhaust gases within the porous medium of the GPF. In proposing a new hybrid model for the fluid flow and the particulate transport, we assume periodicity of the GPF geometry and analyze the flow and transport equations both in the channel and the porous domains. The equations across the two domains are then coupled and create the hybrid model, which tracks particulates at the pore scale and solves for the flow equations at the channel scale, which is several orders of magnitude larger.

For the porous wall, spatially averaged equations are used to model the characteristic pore size. For the flow, the spatially averaged Navier–Stokes equation with the momentum loss term is used, where the loss term accounts for the resistance of the porous wall. For the transport, the spatially averaged advection–reaction equation is adopted, where the reaction term accounts for the particulate trapping. The diffusion and dispersion terms can be neglected in the transport model since the transport is strongly dominated by the advection mechanism [28]. An example of the hybrid approach for the transport in the fractured porous medium is given in [29]. It is shown that the diffusion and dispersion terms can be ignored within the transport equations since the equations are strongly dominated by the advection mechanism. In this paper, we propose to perform the coupling, at different length-scales,

based on the phase indicator function. The coupling of partial differential equations across different domains is a challenging problem [30]. The pore-scale Navier–Stokes equations and the theory of the particle-laden flows (lower-left corner on the scales diagram in Fig. 2) would have generated a computationally costly model mostly associated with the separation of length-scales [26]. The characteristic pore size of the ceramic filter is of the order of $10\,\mu m$, while the length of the wall is a few orders of magnitude bigger (see Table 1). Another factor which challenges the first principle modeling approach, is the uncertainty of the pore-scale geometry. To obtain the detailed pore geometry, one has to scan the porous wall using a micro-CT scanner with a submicron resolution, then process the resulting images with a segmentation algorithm, and finally combine the images to create the three-dimensional (3D) GPF model. This justifies our choice to pursue the development of a hybrid model to generate high fidelity predictions of the flow and transport dynamics inside the GPF.

3 Computational Domain

We consider the ceramic-uncoated GPF of diameter $\bar{D}$ and characteristic pore size $l = 10\,\mu m$. The GPF is composed of a bundle of parallel squared channels of length L and height h_c. The geometric parameters of the GPF used in this study are given in Table 1. A graphical representation of the 3D and two-dimensional (2D) periodic unit is shown in Figs. 3(b) and 3(c), respectively, where the 3D periodic unit is given by the inlet channel surrounded by four halved neighborhood outlet channels and separated by the porous walls, and the 2D periodic unit is obtained by taking the cross section of the 3D periodic unit.

The channels are alternately blocked off by plugs forming a staggered pattern (see Fig. 4). The bundle of the staggered channels can be represented by the collection of spatially distributed periodic units, as shown in Fig. 3(b). The porous medium is
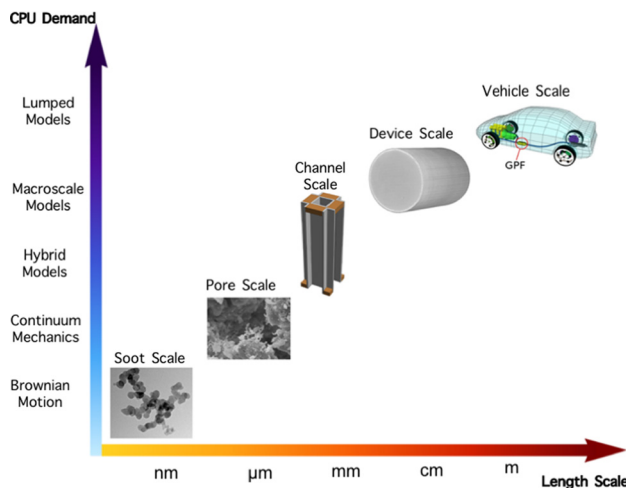

Fig. 2 Computational burden versus length scale diagram of GPF models

Table 1 Geometric characteristics of the uncoated GPF used in this study

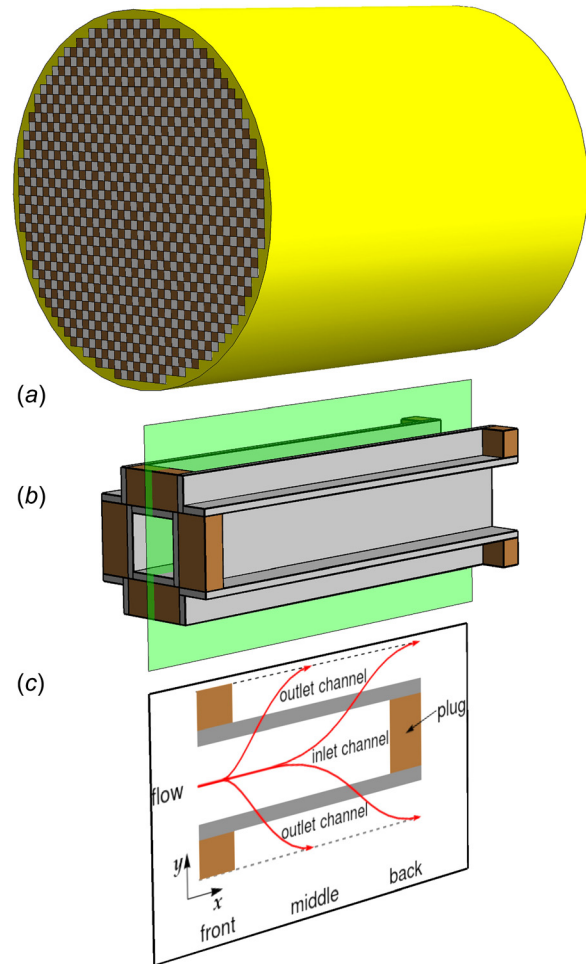| Property	
Material	Cordierite
Diameter	$\bar{D} = 118\,mm$
Length	$L = 127\,mm$
Wall thickness	$h_w = 0.22\,mm$
Channel height	$h_c = 1.03\,mm$
Plug length	$l_p = 7\,mm$

Fig. 3 Schematic representation of (a) GPF, (b) 3D periodic "unit," and (c) longitudinal cross section of the 3D periodic "unit," i.e., 2D periodic "unit"

represented by the representative elementary volume (REV) defined to be the smallest part of the medium that includes all topological features.

The periodicity breaks down at the filter boundary and the accuracy of the periodic representation scales as $\sim 1/\sqrt{N_c}$, where N_c is the total number of channels [31]. To calculate the longitudinal distribution of the deposited particles, we model the dynamics in the longitudinal direction of the 2D cross section of the "unit" shown in Fig. 3(c). A detailed representation of the "unit" cross section is shown in Fig. 5. The inlet channel is plugged at the end, and on the top and the bottom of it, the outlet channels are plugged at the front. The flow and particulates entering the inlet channels go through the porous walls which trap the soot.

The computational domain where the model is evaluated consists of two subdomains, Ω_v and Ω_w, as shown in Fig. 6. The subdomain Ω_v represents the void space of the inlet channels and the subdomain Ω_w represents the porous wall. In the subdomain Ω_v, the first-principle flow and transport equations are used, whereas in the subdomain Ω_w, the upscaled model, or channel model, is employed. We impose the inlet BCs at the left boundary ($\mathcal{B}_l$) and outlet BCs at the right boundary ($\mathcal{B}_r$). The top ($\mathcal{B}_t$) and the bottom ($\mathcal{B}_b$) boundaries have periodic BCs. Around the plugs (the solid walls $\mathcal{W}$ in Fig. 6), the solid wall BCs are imposed.

4 Flow

The incompressible fluid flow is modeled across two spatially separated domains Ω_v and Ω_w. The flow inside the empty channels
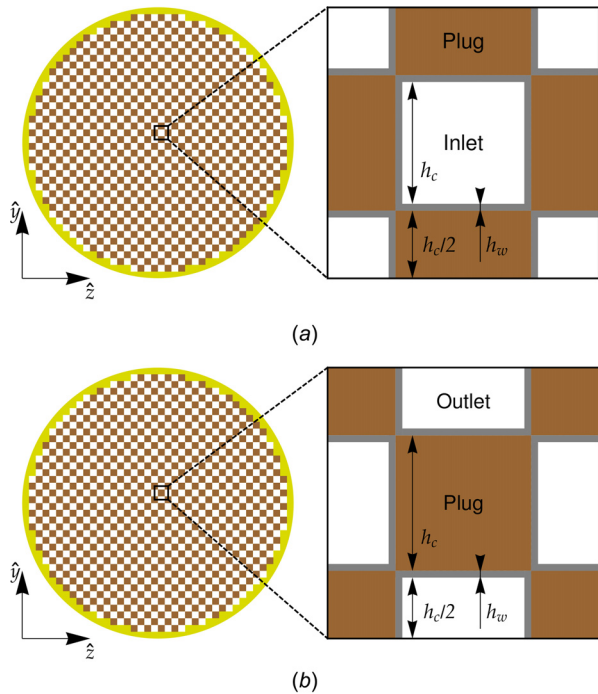
Fig. 4 (a) Top and (b) bottom views of the GPF with their zoomed-in views of inlet/outlet channels and plugs, respectively. The inner square in (a) is the inlet channel whereas the inner square in (b) is the plug. The borders around the inlet channels and the plugs are the porous walls.
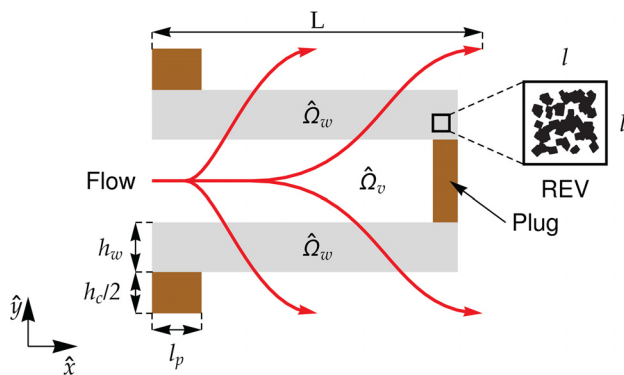

Fig. 5 Schematic representation of the longitudinal cross section of the 2D periodic "unit" and zoomed-in view of REV. The REV size is $l \times l$. The flow enters the channel (subdomain $\hat{\Omega}_v$) and passes through the porous walls (subdomain $\hat{\Omega}_w$).

(subdomain Ω_v) is governed by the Navier–Stokes equation as follows:

$$\frac{\partial \hat{\mathbf{u}}}{\partial \hat{t}} + (\hat{\mathbf{u}} \cdot \hat{\nabla})\hat{\mathbf{u}} = -\frac{1}{\hat{\rho}}\hat{\nabla}\hat{p} + \nu\hat{\nabla}^2\hat{\mathbf{u}}$$
$$\nabla \cdot \hat{\mathbf{u}} = 0, \quad \hat{\mathbf{x}} \in \Omega_v \tag{1}$$

where $\hat{\mathbf{u}}$ is the flow velocity, $\hat{\rho}$ is the fluid density, $\hat{p}$ is pressure, ν is the kinematic viscosity, $\hat{\nabla} = \{\partial/\partial\hat{x}, \partial/\partial\hat{y}\}$ is the gradient operator, and $\hat{\mathbf{x}} = \{\hat{x}, \hat{y}\}$ indicate the two-dimensional spatial coordinates. The compressibility effects are neglected since the flow velocity is orders of magnitude smaller than the speed of sound. For the flow inside the porous wall $\hat{\Omega}_w$, we use the spatially averaged Navier–Stokes equation with the moment loss term as follows
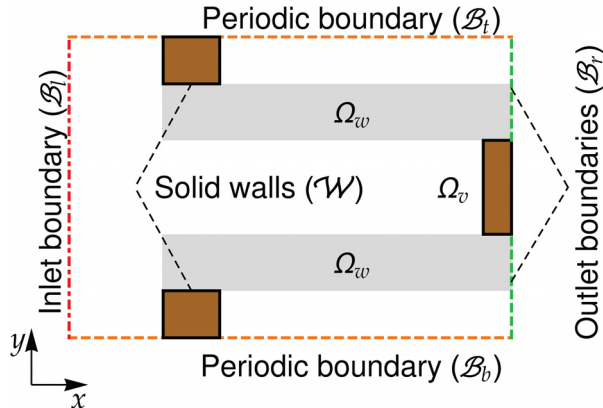

Fig. 6 Schematic plot of the computational domain used to develop the hybrid model of GPF. The dot-dashed vertical lines show the inlet boundary ($\mathcal{B}_l$), the outlet boundaries ($\mathcal{B}_r$), and the periodic boundaries ($\mathcal{B}_b$, $\mathcal{B}_t$), along with the plugs. The solid lines framing the plugs represent the solid wall (nonpenetrable) boundaries ($\mathcal{W}$). The porous subdomain Ω_w and the void space subdomain Ω_v are also shown.

$$\frac{\partial \langle\hat{\mathbf{u}}\rangle}{\partial \hat{t}} + \left(\langle\hat{\mathbf{u}}\rangle \cdot \hat{\nabla}\right)\langle\hat{\mathbf{u}}\rangle = -\frac{1}{\hat{\rho}}\hat{\nabla}\langle\hat{p}\rangle + \nu\hat{\nabla}^2\langle\hat{\mathbf{u}}\rangle - \frac{\nu}{\hat{k}}\langle\hat{\mathbf{u}}\rangle\nabla \cdot \langle\hat{\mathbf{u}}\rangle = 0,$$
$$\hat{\mathbf{x}} \in \Omega_w \tag{2}$$

where $\hat{k}$ is the porous medium permeability and $\langle\cdot\rangle$ denotes the volume averaging over the fluid phase of the REV. Nonlocal terms are neglected in Eq. (2). We assume that the permeability does not change during particulate accumulation. Equations (1) and (2) are supported by the proper boundary conditions on the domains Ω_v and Ω_w.

The following dimensionless quantities are used from now on

$$\mathbf{v} = \hat{\mathbf{v}}/u_{\text{in}}, \quad t = \hat{t}/(h_c/u_{\text{in}})$$
$$\mathbf{x} = \hat{\mathbf{x}}/h_c, \quad p = \hat{p}/(\rho u_{\text{in}}^2) \tag{3}$$

where u_{in} is the horizontal component of the velocity at the inlet and h_c is the width of the inlet channel (see Table 1). Combining Eqs. (1) and (2) into a single hybrid equation written in terms of the dimensionless quantities (3) yields to

$$\frac{\partial \bar{\mathbf{u}}}{\partial t} + (\bar{\mathbf{u}} \cdot \nabla)\bar{\mathbf{u}} = -\nabla\bar{p} + \frac{1}{\text{Re}}\nabla^2\bar{\mathbf{u}} - \frac{\alpha(\mathbf{x})}{\text{Re}}\frac{1}{k}\bar{\mathbf{u}}$$
$$\nabla \cdot \bar{\mathbf{u}} = 0, \quad \mathbf{x} \in \Omega_c \cup \Omega_w \tag{4}$$

where $\text{Re} = u_{\text{in}}h_c/\nu$ is the Reynolds number and $\alpha(\mathbf{x})$ is the indicator function. When $\mathbf{x} \in \Omega_c$, $\alpha = 0$, whereas when $\mathbf{x} \in \Omega_w$, $\alpha = 1$. The hybrid velocity $\bar{\mathbf{u}}$ models the flow velocity, $\mathbf{u}$, in the empty channels when $\alpha = 0$ and the average flow velocity in the porous medium $\langle\mathbf{u}\rangle$ when $\alpha = 1$. Equation (4) is supported by the boundary conditions (see Fig. 6)

$$\bar{u}_x = 1, \quad \frac{\partial \bar{p}}{\partial x} = 0, \quad \mathbf{x} \in \mathcal{B}_l$$
$$\bar{\mathbf{u}} = 0, \quad \mathbf{x} \in \mathcal{S}$$
$$\mathbf{n} \cdot \nabla\bar{\mathbf{u}} = 0, \quad \bar{p} = 0, \quad \mathbf{x} \in \mathcal{B}_r \tag{5}$$
$$\bar{\mathbf{u}}(\mathbf{x})|_{\mathbf{x}\in\mathcal{B}_b} = \bar{\mathbf{u}}(\mathbf{x})|_{\mathbf{x}\in\mathcal{B}_t}, \quad \bar{p}(\mathbf{x})|_{\mathbf{x}\in\mathcal{B}_b} = \bar{p}(\mathbf{x})|_{\mathbf{x}\in\mathcal{B}_t}$$

The volume-averaged flow velocity magnitude inside the porous domain is given by

$$\mathcal{U}_{\text{filtration}} = \frac{1}{|\Omega_w|}\int_{\Omega_w} |\bar{\mathbf{u}}(x, y, t)|dxdy \tag{6}$$

and inside the empty channels by

$$\mathcal{U}_{\text{channel}} = \frac{1}{|\Omega_v|} \int_{\Omega_v} |\bar{\mathbf{u}}(x,y,t)| dx dy \quad (7)$$

where $|\Omega_w|$ and $|\Omega_v|$ are the volumes of the porous and void domains, respectively. Moreover, the average pressure at the inlet is given by

$$\mathcal{P}_{\text{inlet}} = \frac{1}{2(h_c + h_w)} \int_{\mathcal{B}_l} p(\mathbf{x}, t) d\mathbf{x} \quad (8)$$

and the longitudinal distribution of the velocity magnitude inside the porous wall by

$$U(x,t) = \frac{1}{2h_w} \int_{\Omega_w} |\bar{\mathbf{u}}(x,y,t)| dy \quad (9)$$

5 Particulate Transport

The particulate transport in the empty channels (subdomain Ω_v) follows the advection–diffusion equation

$$\frac{\partial \hat{c}}{\partial \hat{t}} = \hat{\nabla} \cdot (D \hat{\nabla} \hat{c}) - \hat{\nabla} \cdot (\hat{\mathbf{u}} \hat{c}) \quad \hat{\mathbf{x}} \in \hat{\Omega}_v \quad (10)$$

where $\hat{c}$ is the particulate concentration, D is the particulate diffusion coefficient, and $\hat{\mathbf{u}}$ is the flow velocity defined by Eq. (1). Rewriting Eq. (10) in terms of the dimensionless quantities in Eq. (3) yields to a dimensionless form of the transport equation

$$\frac{\partial c}{\partial t} = \frac{1}{\text{Pe}_c} \nabla \cdot \nabla c - \nabla \cdot (\mathbf{u} c)$$
$$\mathbf{x} \in \Omega_v \quad (11)$$

where $\text{Pe}_c = h_c u_{\text{in}}/D$ is the Péclet number of the transport in the empty channels and the concentration is rescaled as $c = \hat{c}/c_{\text{in}}$, where c_{in} is the concentration at the domain's inlet.

The characteristic value of particulate diffusion inside the fluid can be estimated by the Stokes–Einstein equation

$$D = \frac{k_B T}{6\pi\nu\rho r} \quad (12)$$

where k_B is Boltzmann's constant, T is the fluid temperature, and r is the particle's radius.

For a characteristic radius of the soot particle of $r = 50$ nm, characteristic temperature of the fluid in the exhaust pipe of $T = 600$ K, flow velocity of $u_{\text{in}} = 10$ m/s, and kinematic viscosity of air of $\nu = 51.29 \times 10^{-6}$ m^2/s and air density of $\rho = 0.59$ kg/m^3, the estimated value of the Péclet number is $\text{Pe}_c = 3.55 \times 10^7$, which corresponds to the advection-dominated transport regime. Thus, the diffusion can be neglected in Eq. (10) and the transport is governed by the advection equation

$$\frac{\partial c}{\partial t} = -\nabla \cdot (\mathbf{u} c) \quad \mathbf{x} \in \Omega_v \quad (13)$$

Analyzing the macroscale transport equation for the porous walls (subdomain Ω_w) is not straightforward, since the pore-scale advection term contributes to the macroscale dispersion tensor $D^\star$ [32]. For such analysis, the asymptotic theory developed in Ref. [33] is used. Starting from the pore scale analysis, the transport is governed by the advection–diffusion equation with the Neumann boundary condition as follows:

$$\frac{\partial c}{\partial t} = \frac{1}{\text{Pe}_w} \nabla \cdot \nabla c - \nabla \cdot (\mathbf{u} c) - \mathbf{n} \cdot \nabla c = \text{Da} c \quad (14)$$

where the spatial coordinate is rescaled to the thickness of the porous wall $\mathbf{x} = \hat{\mathbf{x}}/h_w$, the velocity is rescaled to the characteristic pore-scale velocity u_w, the Péclet number is $\text{Pe}_w = h_w u_w/D$, and $\mathbf{n}$ is the normal vector to the fluid/surface interface. The boundary condition in Eq. (14) accounts for the particulate collection in the wall surface. Damköhler number in the boundary condition $\text{Da} = h_w K/D$ defines the ratio of the particulate collection and diffusion time scales where K is the rate of the particulate collection. By introducing the scales separation parameter ε, the transport equation can be written as [33]

$$\frac{\partial c}{\partial t} = \varepsilon^m \nabla \cdot \nabla c - \nabla \cdot (\mathbf{u} c) \quad (15)$$

where ε is the ratio of the pore-scale and the thickness of the porous wall, namely, $\varepsilon = l/h_w$. The power of ε, m, defines the type of the macroscale equation for the porous wall. If m is greater than 2, the dispersion term can be neglected in the macroscale equation, i.e., $D^\star \nabla \cdot \nabla \langle c \rangle \sim 0$ [32].

From the characteristic pore size of the porous wall of $l = 10\,\mu\text{m} = 10^{-5}$ m, the scales separation parameter is equal to $\varepsilon = 0.0454$. The estimated flow velocity in the porous wall, u_w, is 139 times less (see Table 2) than the velocity in the inlet channel, $u_w = 0.072$ m/s, where the velocity u_w was estimated by the numerical solution of Eq. (4). The Péclet number for the porous wall is $\text{Pe}_w = 5.43 \times 10^4$ and the power of ε is equal to $m = -\log(\text{Pe}_w)/\log(\varepsilon) = 3.52$. Thus, the dispersion for the macroscale transport can be neglected and the transport inside the porous wall is governed by the dimensioned advection–reaction equation

$$\frac{\partial \langle \hat{c} \rangle}{\partial \hat{t}} = -\hat{\nabla} \cdot (\langle \hat{\mathbf{u}} \rangle \langle \hat{c} \rangle) - \hat{K} \langle \hat{c} \rangle \quad \hat{\mathbf{x}} \in \Omega_w \quad (16)$$

where $\hat{K}$ is the dimensioned rate of the particulate collection. In Eq. (16), the nonlocal memory effect is neglected [33]. Equation (16) is rescaled using the concentration at the domain inlet c_{in} and quantities introduced in Eq. (3). Finally, the dimensionless macroscale transport equation for the porous walls is

$$\frac{\partial \langle c \rangle}{\partial t} = -\nabla \cdot (\langle \mathbf{u} \rangle \langle c \rangle) - K \langle c \rangle \quad \mathbf{x} \in \Omega_w \quad (17)$$

where the particulate collection rate is rescaled as $K = \hat{K}/(u_{\text{in}}/h_c)$.

Finally, combining Eqs. (13) and (17) by means of the indicator function $\alpha(\mathbf{x})$ yields to the hybrid equation

$$\frac{\partial \bar{c}}{\partial t} = -\nabla \cdot (\bar{\mathbf{u}} \bar{c}) - \alpha K \bar{c} \quad \mathbf{x} \in \Omega_c \cup \Omega_w \quad (18)$$

where $\bar{\mathbf{u}}$ is governed by Eq. (4). Equation (18) is supported by the boundary conditions

$$\bar{c} = 1, \quad \mathbf{x} \in \mathcal{B}_l$$
$$\mathbf{n} \cdot \nabla \bar{c} = 0, \quad \mathbf{x} \in \mathcal{S}$$
$$\frac{\partial \bar{c}}{\partial x} = 0, \quad \mathbf{x} \in \mathcal{B}_r \quad (19)$$
$$\bar{c}(\mathbf{x})|_{\mathbf{x} \in \mathcal{B}_b} = \bar{c}(\mathbf{x})|_{\mathbf{x} \in \mathcal{B}_t}$$

The filtration efficiency is defined as one minus the ratio of particulate flux at the outlet over the flux at the inlet

$$\Phi = 1 - \frac{\int_{\mathcal{B}_r} \bar{u}_x \bar{c}\, dx}{\int_{\mathcal{B}_l} dx} \quad (20)$$

where $\bar{u}_x$ is the x component of the flow velocity, $\bar{c}$ is the normalized concentration, and the x component of the flow velocity is 1

at the inlet. The filter has zero efficiency when the two fluxes are equal.

Since the particulate absorption is proportional to the concentration, we calculate the longitudinal distribution, C, of the deposited particles as

$$C(x,t) = \frac{1}{2h_w}\int_{\Omega_w} \bar{c}(x,y,t)dy \qquad (21)$$

The flow and the transport problems are solved numerically to estimate the key parameters of the filtration, such as the filtration velocity (see Eq. (6)), $\mathcal{U}_{\text{filtration}}$, the filtration efficiency, Φ.

6 Numerical Simulations

We numerically solve the flow and the transport equations, Eqs. (4) and (18), with the boundary conditions expressed by Eqs. (5) and (19) using the finite volume framework Open source Field Operation And Manipulation (OPENFOAM). OPENFOAM is a C++ toolbox for the development of customized numerical solvers and solution of continuum mechanics problems including computational fluid dynamics. OPENFOAM includes the mesh utilities, customizable solvers of partial differential equations, and postprocessing utilitie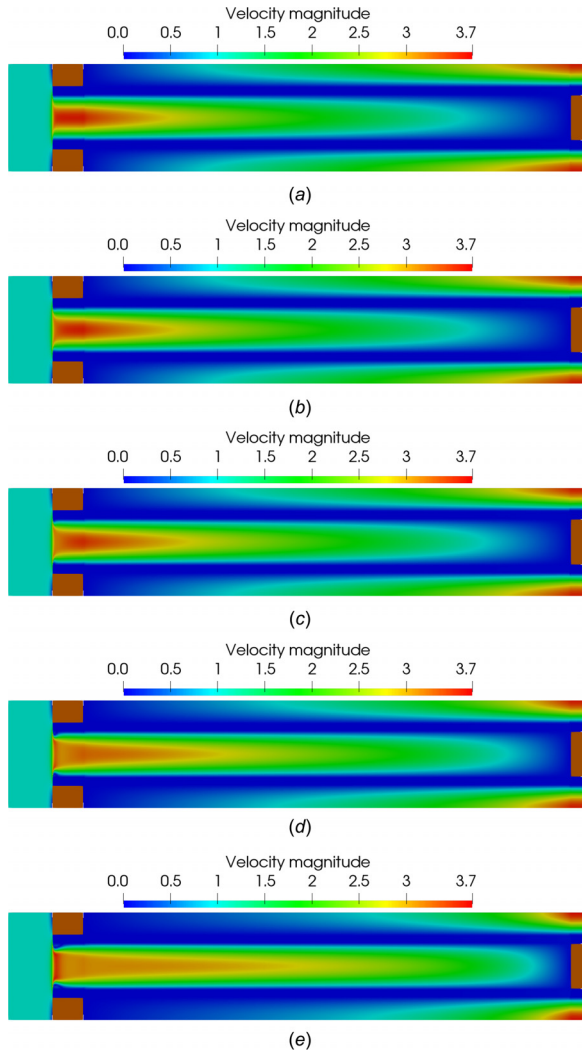s. We create the solver for the hybrid flow equation by modifying the large time-step transient solver for incompressible flow *pimpleFOAM*. For the solution of the hybrid transport equation, we modify the advection–diffusion solver *transportFOAM*.

We create the Cartesian computational mesh using the *block-Mesh* utility. The lower right point of the mesh has coordinates $(x,y) = (-10, -1.2135)$ and the upper right point $(x,y) = (119.9029, 1.2135)$. The x coordinate of the central inlet is 0. The mesh has 5252 cells along the x direction and 100 cells along the y direction. Using the *snappyHexMesh* utility, we define the plugs inside the mesh. For the mesh preparation, we use the standard set of parameters [34]. The flow simulations were run using the five values of Reynolds number

$$\text{Re} = \{20, 50, 100, 250, 500\}$$

The above characteristic values of Re used in the simulations were estimated from the lowest or highest values of the mass flow rate and the exhaust temperature reported in Galindo et al. [35] and the diameter of the GPF from Table 1. These values are characteristic of the vehicle exhaust system [24].
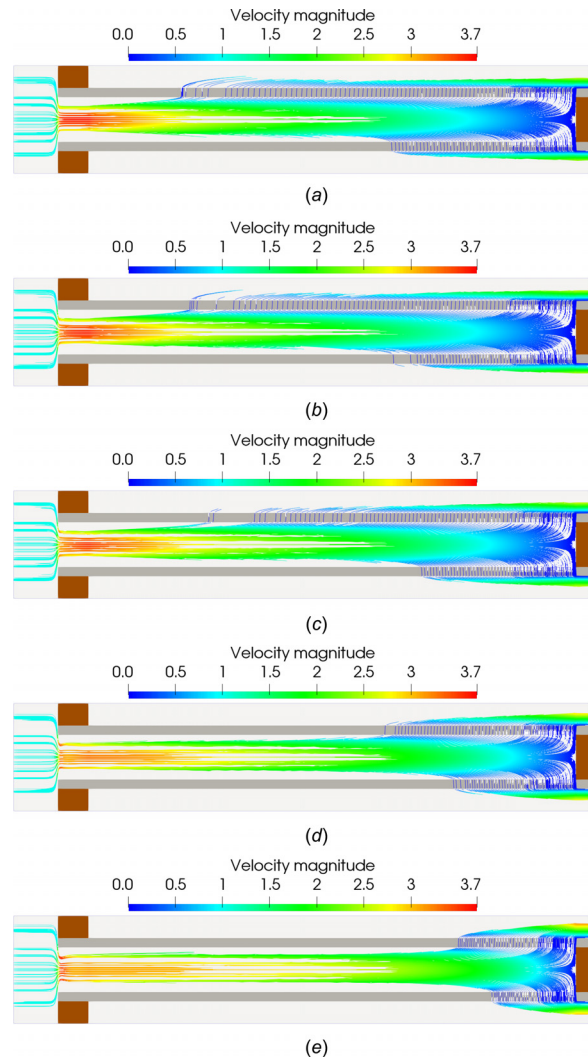

Fig. 7 Steady-state distribution of the flow velocity magnitude for Re = {20, 50, 100, 250, 500}. The plugs are indicated by the brown rectangles. (*a*) Re = 20, (*b*) Re = 50, (*c*) Re = 100, (*d*) Re = 250, and (*e*) Re = 500.

Fig. 8 The color-coded streamline plot of the steady-state flow for Re = {20, 50, 100, 50, 500} as a function of the velocity magnitude. The dark gray regions indicate the location of the porous walls whereas the brown rectangles indicate the plugs. (*a*) Re = 20, (*b*) Re = 50, (*c*) Re = 100, (*d*) Re = 250, and (*e*) Re = 500.
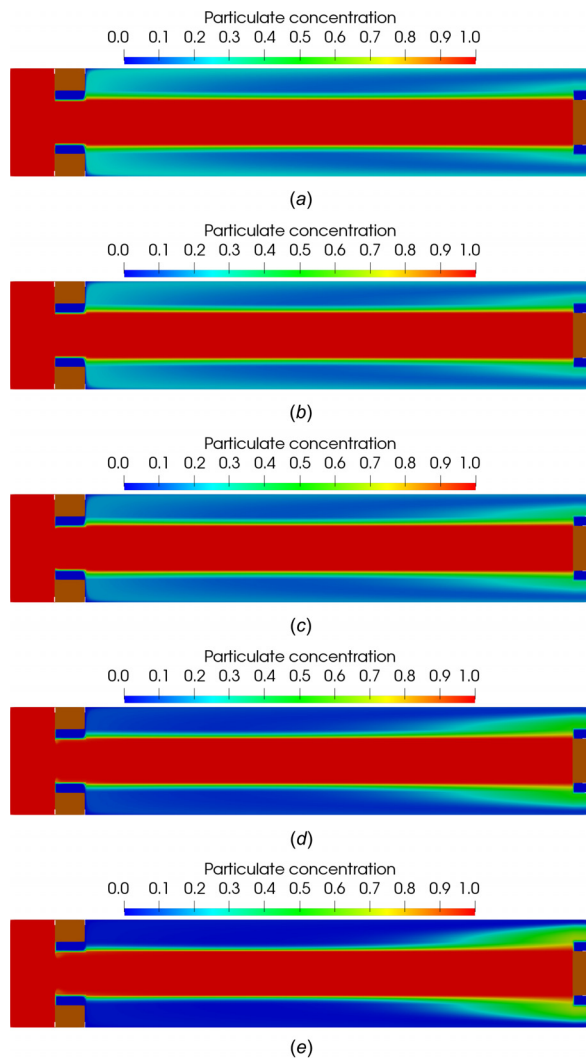
(a)

(b)

(c)

(d)

(e)

Fig. 9 Steady-state particulates concentration distribution for Re = {20, 50, 100, 250, 500}. (a) Re = 20, (b) Re = 50, (c) Re = 100, (d) Re = 250, and (e) Re = 500.

The permeability of the filter porous walls, k, was estimated based on the permeability value of the clean GPF from Ref. [18]. The results of the flow simulations are shown in Figs. 7 and 8. Because of the initial aspect ratio the computational domain is $2.5/127$. For illustration purposes, the images are rescaled to the
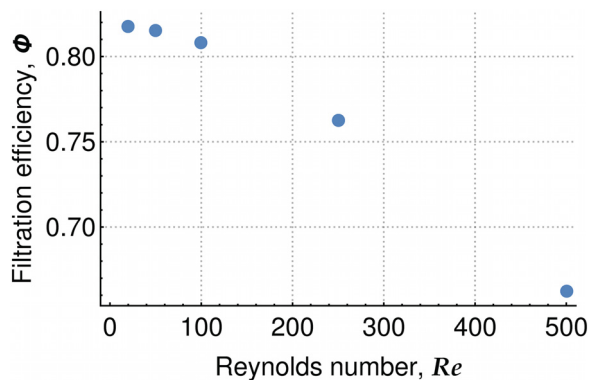

Fig. 10 Filtration efficiency versus Reynold number calculated from the steady-state numerical solution of the transport model. The exact numerical values are shown in the last row of Table 2.

Table 2 Volume-averaged flow velocity magnitude inside the porous walls, volume-averaged flow velocity magnitude inside the void space, average pressure at the inlet, and filtration efficiency for various values of the Reynolds number

	Re = 20	Re = 50	Re = 100	Re = 250	Re = 500
$\mathcal{U}_{\text{filtration}}$	9.3×10^{-3}	9.3×10^{-3}	9.3×10^{-3}	9.5×10^{-3}	9.5×10^{-3}
$\mathcal{U}_{\text{channel}}$	1.29	1.32	1.39	1.53	1.74
$\mathcal{P}_{\text{inlet}}$	166.74	69.56	37.42	18.82	13.47
Filtration efficiency, Φ	0.817	0.815	0.808	0.762	0.663

The parameters were calculated using Eqs. (6)–(8) and the steady-state numerical solution of the flow model. The filtration efficiency was calculated using Eq. (20).
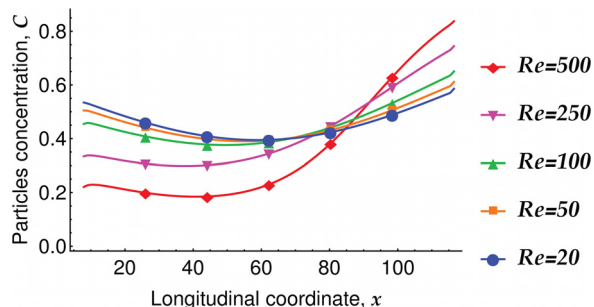

Fig. 11 Longitudinal concentration of the particles inside the porous walls (subdomain Ω_w) calculated from the steady-state numerical solution of the transport model. This shows how driving conditions, in the form of mass flowrate changes, affect the particulate deposition along the filter.

aspect ratio 25/127. The simulations of the flow and transport equations converge to the steady-state solution with an accuracy of 1×10^{-6}.

The streamline plot in Fig. 8 shows the direction of the fluid flow. The streamlines are noticeably denser at the back end of the inlet channel. This effect increases with the Reynolds number. The streamline plots also show the path of the particulate transport in the advective transport regime. Particulate is forced to pass through the porous walls toward the back end of the channel. This phenomenon has also been observed in the literature [12,18]. Despite the domain and the boundary conditions being symmetric, the steady-state solutions are asymmetric. Notwithstanding what intuition might lead to think, the periodic boundary condition assumption does not resolve into a symmetric behavior. In fact, the breaking of the flow symmetry in a channel with sudden contraction/expansion is confirmed by the numerical and experimental investigation conducted in Ref. [36]. The steady-state particulate concentration is shown in Fig. 9. The dimensionless value
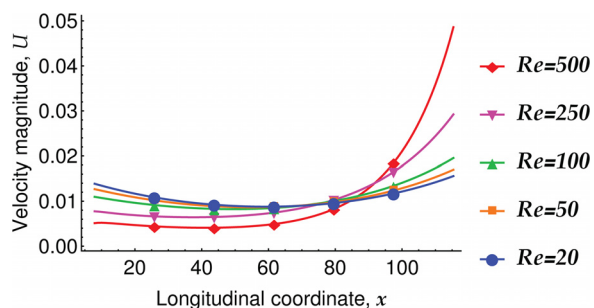

Fig. 12 Longitudinal velocity magnitude inside the porous walls (subdomain Ω_w) calculated from the steady-state numerical solution of the transport model
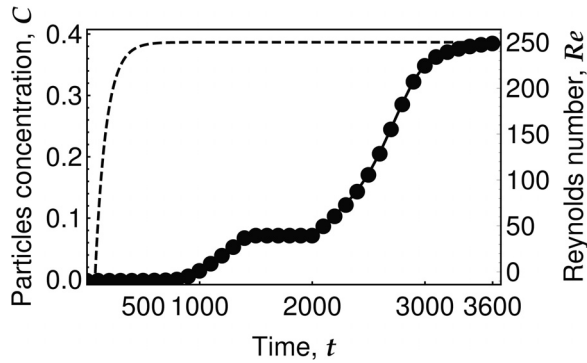
Fig. 13 Concentration of particles inside the porous wall over time (dashed line) as Reynolds number at the inlet changes in time according to the staircase type of profile (circles and solid line)
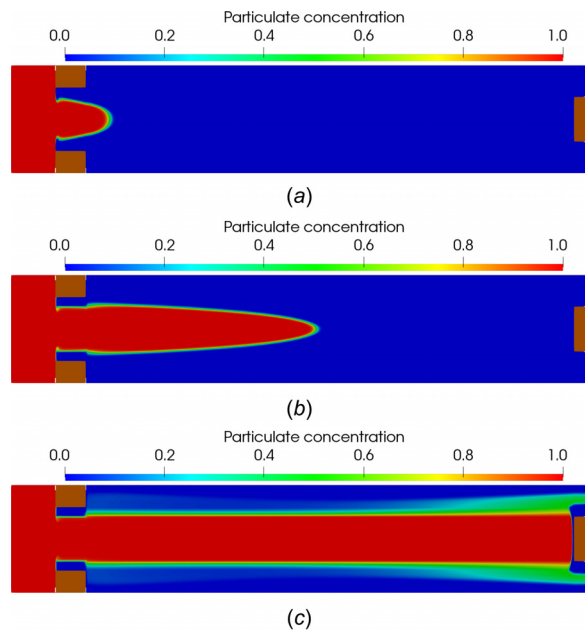

Fig. 14 Spatial distribution of particulate concentration during transient simulations: (*a*) *t* = 500, (*b*) *t* = 1000, and (*c*) *t* = 3600

of the particulate collection rate was set to $K = 0.1$, which corresponds to a filtration efficiency approximately equal to 0.8. Using Eqs. (20) and (9), the filtration efficiency, the longitudinal distribution of the deposited particles, and the spatial distribution of the velocity magnitude for different Reynolds numbers are calculated and shown in Figs. 10–12, respectively.

Transient simulations of the flow and particulate transport were conducted where the flow velocity at the inlet was set in such a way that the Reynolds number was following a staircase type of function—as a function of time (see Fig. 13). Simulations were run until the solution reached steady-state. The spatial distribution of particulate concentration at three different time instants is shown in Fig. 14.

7 X-Ray Computed Tomography Scan

X-ray computed tomography (XCT) scanning is a widely used technique for nondestructive and noninvasive 3D imaging of a solid sample. The output of the XCT experiment provides a 3D distribution of the relative attenuation of the scattered X-ray beam, where the beam intensity depends on the distribution of the sample density.
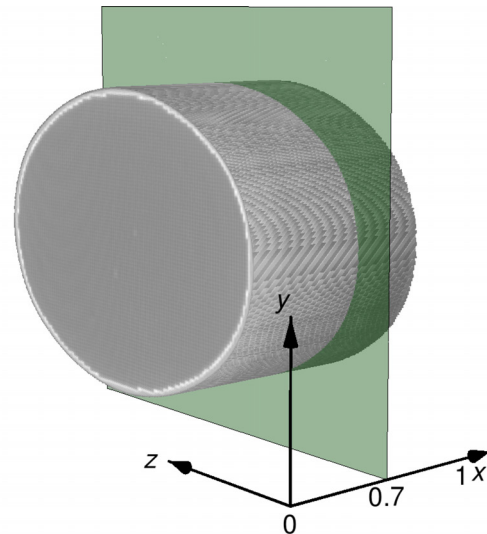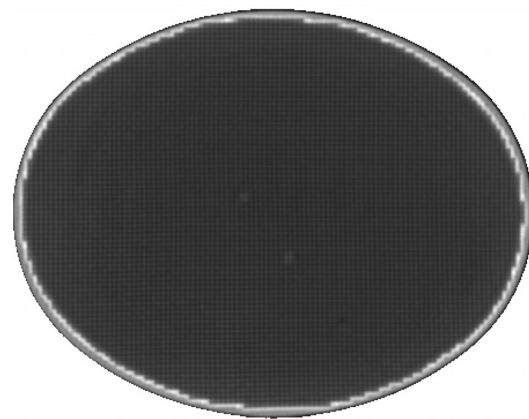
Fig. 15 (*a*) Volumetric render from the XCT images of the clean filter and cross section image (*b*) obtained from the coordinate where the green plane is shown in (*a*). (*a*) Volumetric render and (*b*) image.

To obtain the longitudinal distribution of the deposited particles, we perform XCT scanning over a clean and soot-loaded filter. The scanning was performed using the General Electric HiSpeed CT/i X-ray scan at Stanford University, Stanford, CA. For the GPF under study, the achieved axial resolution of the imaging is approximately 0.3×0.3 mm and the longitudinal resolution approximately 3 mm. The scanner has a dedicated laser positioning system that allows accurate 3D slice-wise scanning, which is performed in the axial plane. The intensity of the X-ray beam is suitably adjusted to achieve the best possible contrast. As a result, scanning experiment outputs a pile of gray-scale images, where each image shows the distribution of the GPF density at a given axial plane location. The 3D renders from the XCT images of the fresh and the soot-loaded filters and examples of the single images are shown in Figs. 15 and 16. The imaging scanning experiment for the clean GPF produced 35 images, whereas for the soot-loaded GPF, 27 images were obtained. The dimension of each image was 512×512 pixels. The results of the XCT scan can be represented as a 3D array, $\mathcal{I}$, as follows:

$$\mathcal{I} = \{v_{ijk}, i = 1, .., N_x, j = 1, .., N_y, k = 1, ..., N\} \quad (22)$$

where v_{ijk} is the gray-scale intensity for the pixel with coordinate i, j for the kth image, N_x and N_y are the image dimensions, and N
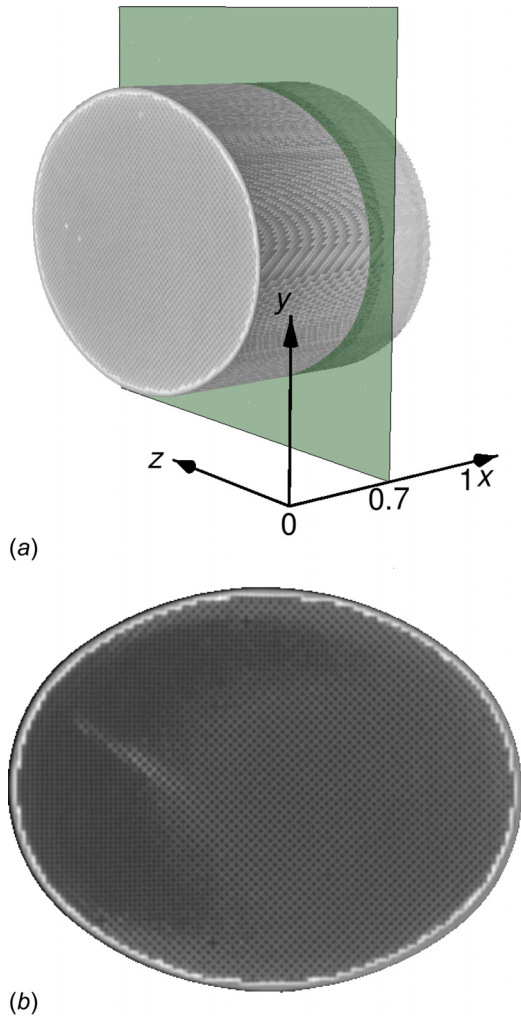
(a)

(b)

Fig. 16 (*a*) **Volumetric render from the XCT images of the soot-loaded filter, and cross section image** (*b*) **obtained from the coordinate where the green plane is shown in** (*a*). (*a*) **Volumetric render and** (*b*) **image.**

is overall number of images. The first image, $k = 1$, corresponds to the frontal face of the filter, while the last image, $k = N$, to the back of the filter.

To identify the longitudinal distribution of the deposited particles, images containing the plugs were excluded. Following the image rearrangement process, the subscript $k = 1$ is used to indicate the first slice after the plugs and $k = N$ the last slice before the plugs. Finally, the images were postprocessed by subtracting the average intensity of the first image from the average intensity of each image

$$ I_k = \frac{1}{N_x N_y} \sum_{i=1}^{N_x} \sum_{j=1}^{N_y} v_{ijk} - I_1 \qquad (23) $$

The discrete nature of the photons and the thermal fluctuations of electrons of the electronic components introduce noise in the XCT images. Such a noise is Gaussian in nature with zero mean [37]. As an implication, images taken at the same location show fluctuation in pixel intensity. Moreover, output from XCT experiment is an ergodic and stationary process. The ergodicity property guarantees the same behavior averaged in time and space, and the probability density function of pixel intensity related to the same density of the sample is also Gaussian. Moreover, the noise from the XCT experiment cancels out after the average procedure. The accuracy of the averaged quantities estimated from XCT
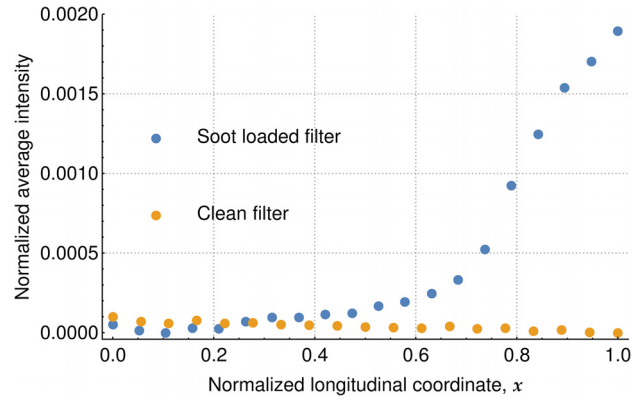

Fig. 17 Relative particle concentration inside the GPF along the normalized x direction for the clean and soot-loaded filters. $x = 0$ is the coordinate at which the first image is taken at the front of the filter after the plug and $x = 1$ is the coordinate of the last image at the back end before the plug.

experiment was shown in Ref. [38] where a comparison of the porosity value estimated from the image processing and the direct experiment was conducted.

Figure 17 shows the image average intensity I_k for the clean and soot-loaded filters. The XCT measurements are consistent with the concentration distribution predicted by the proposed model showing that particulates tend to accumulate more toward the back end of the filter. The clean filter shows almost no change in the average intensity.

8 Conclusions and Future Work

In this paper, we have proposed a hybrid model for the flow and particle transport dynamics in GPFs by using the concept of periodic unit cell and by coupling equations for the empty channel with averaged equations for the porous wall using the indicator function approach. Simulation results show that the proposed model captures the nonuniform distribution of the particulate deposition, the dependence of the filtration efficiency on Reynolds number, and the particle concentration distribution along the longitudinal coordinate. In designing the proposed model, the particulate trapping rate value, K, was treated as an input parameter for the simulation study. In future work, we plan to conduct experiments aimed at estimating the values of K across different filter operations. In particular, we plan to determine the breakthrough curve of the filter under different flow operating conditions. Moreover, the results obtained in simulations, confirming the experimental evidence that the filtration efficiency is not uniform along the entire filter length, have motivated us to investigate alternative filter designs. Using the proposed hybrid model, we are showing that a new internal geometry of the channel could lead to an improved filtration efficiency. This is detailed in Sec. 8.1.

8.1 A New Channel Design to Improve Filtration Efficiency. We expand the numerical analysis shown so far to investigate how improvement of the filtration efficiency could be achieved through a modified geometry of the inlet channel. The new geometry accounts for placing small solid pins on the surface of the porous wall of the inlet channel with the aim of redistributing uniformly the flow inside the porous wall. The pins create an additional momentum perpendicular to the porous wall, which enforces the flow to be redistributed uniformly in the porous wall. Such a design has the aim of increasing the effective filtration surface of the porous wall. We conducted two simulations scenarios, both at Reynolds number of 250. In the first scenario, the pins are placed both on the top and the bottom of the channel at the same spatial location, whereas in the second scenario, the pins are alternately spaced and placed on the top and the bottom of the channel.
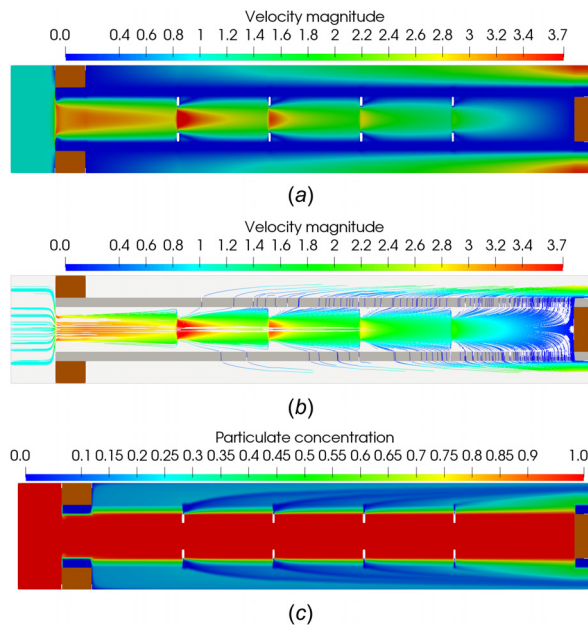
Fig. 18 Steady-state distribution of the flow velocity magnitude (*a*), streamlines (*b*), and particulates concentration (*c*) in the GPF channel with the new geometry under Re = 250 condition. Pins are placed at the same location both at the bottom and top of the channel. The brown rectangles indicate the plugs and white small rectangles indicate the pins. (*a*) Velocity magnitude, (*b*) streamlines, and (*c*) particulates concentration.
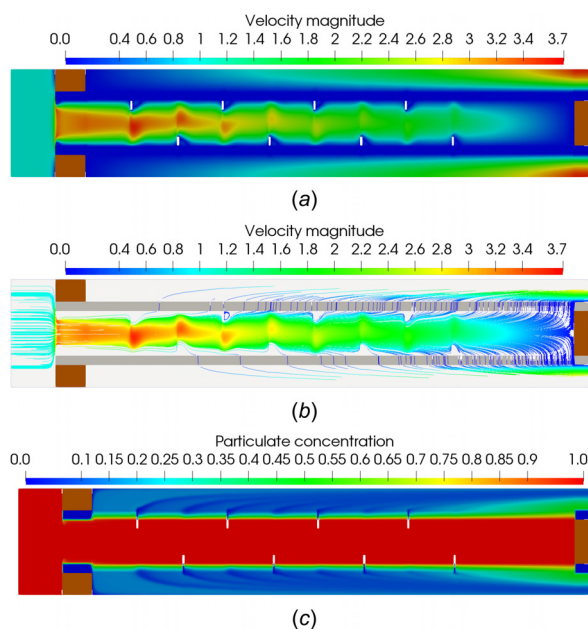

Fig. 19 Steady-state distribution of the flow velocity magnitude (*a*), streamlines (*b*), and particulates concentration (*c*) in the GPF channel with the new geometry under Re = 250 condition. Pins are alternately placed both at the bottom and top of the channel. The brown rectangles indicate the plugs and white small rectangles inside the channel indicate the pins. (*a*) Velocity magnitude, (*b*) streamlines, and (*c*) particulates concentration.

Each pin has a normalized height and width of 0.2 and 0.5, respectively.[3] Simulations are conducted to calculate the steady-state flow velocity distribution, steady-state particulate concentration

---

distribution, and the filtration efficiency according to Eq. (20). The average pressure at the inlet is also estimated to ensure that the inclusion of the pins does not create high back-pressure. The filtration efficiency of the channel for the standard configuration without pins and the new ones with pins is calculated. For both scenarios, the filtration efficiency is 0.78, which results in a 2% improvement when compared to the case of channel without pins (see Table 2). For the channel with pins equally spaced (at the bottom and the top of the channel), the average pressure at the inlet is 20.20 and for the channel with pins alternately placed the average pressure at the inlet is 19.57. Simulation results for the first and second scenarios are shown in Figs. 18 and 19, respectively. A systematic model-based optimization study aimed at improving the filtration efficiency through the new design by exploiting the hybrid model presented in this paper is the subject of future investigation.

Nomenclature

$\mathcal{B}_b$ = bottom boundary of the computational domain
$\mathcal{B}_l$ = left boundary of the computational domain
$\mathcal{B}_r$ = right boundary of the computational domain
$\mathcal{B}_t$ = top boundary of the computational domain
$\bar{c}$ = particulate concentration (kg/m^3)
c_{in} = particulate inlet concentration (kg/m^3)
D = particulate diffusion constant (m^2/s)
$\bar{D}$ = diameter of GPF (m)
Da = Damkohler number of the particulate absorption
h_c = height of the channel (m)
h_w = thickness of the porous wall (m)
K = particulate trapping rate
$\hat{k}$ = permeability (m^2)
$\hat{K}$ = particulate trapping rate (1/s)
k_B = Boltzmann's constant (J/K)
l = pore size (m)
L = length of GPF (m)
l_p = length of the plug (m)
n = normal vector
N_c = number of channels
$\bar{\mathbf{p}}$ = coupled pore- and macro-scales pressures
$\hat{p}$ = pressure (Pa)
$\langle \hat{p} \rangle$ = macroscale pressure (Pa)
Pe_c = Peclet number for the channel
Pe_w = Peclet number for the porous wall
r = particle radius (m)
$\mathcal{S}$ = solid wall boundary of the computational domain
T = fluid temperature (K)
$\hat{t}$ = time (s)
$\hat{\mathbf{u}}$ = pore-scale velocity (m/s)
$\langle \hat{\mathbf{u}} \rangle$ = macroscale velocity (m/s)
$\bar{\mathbf{u}}$ = coupled pore- and macro-scales velocities
u_{in} = horizontal component of the inlet velocity (m/s)
$\mathbf{x}$ = coordinate
x = horizontal coordinate
$\hat{x}$ = horizontal coordinate (m)
y = vertical coordinate
$\hat{y}$ = vertical coordinate (m)
α = void/porous space indicator function
∇ = gradient operator
$\hat{\nabla}$ = gradient operator (1/m)
ε = scales separation parameter
ν = fluid kinematic viscosity (m^2/s)
ρ = fluid density (g/m^3)
ϕ = porosity
Ω_v = void space of the computational domain

$\Omega_w =$ porous space of the computational domain
Re $=$ Reynolds number

References

[1] Maricq, M. M., and Xu, N., 2004, "The Effective Density and Fractal Dimension of Soot Particles From Premixed Flames and Motor Vehicle Exhaust," J. Aerosol Sci., **35**(10), pp. 1251–1274.

[2] Stanmore, B. R., Brilhac, J. F., and Gilot, P., 2001, "The Oxidation of Soot: A Review of Experiments, Mechanisms and Models," Carbon, **39**(15), pp. 2247–2268.

[3] Eastwood, P., 2008, *Particulate Emissions From Vehicles*, Vol. 20, Wiley, Hoboken, NJ.

[4] Kleeman, M. J., Schauer, J. J., and Cass, G. R., 2000, "Size and Composition Distribution of Fine Particulate Matter Emitted From Motor Vehicles," Environ. Sci. Technol., **34**(7), pp. 1132–1142.

[5] Demuynck, J., Favre, C., Bosteels, D., Hamje, H., and Anderson, J., 2017, "Real-World Emissions Measurements of a Gasoline Direct Injection Vehicle Without and With a Gasoline Particulate Filter," SAE Paper No. 2017-01-0985.

[6] Santillo, M., Magner, S., Uhrich, M., and Jankovic, M., 2015, "Towards Ecu-Executable Control-Oriented Models of a Three-Way Catalytic Converter," ASME Paper No. DSCC2015-9653.

[7] Konstandopoulos, A. G., Kostoglou, M., Skaperdas, E., Papaioannou, E., Zarvalis, D., and Kladopoulou, E., 2000, "Fundamental Studies of Diesel Particulate Filters: Transient Loading, Regeneration and Aging," SAE Paper No. 2000-01-1016.

[8] Zhu, R., Hu, J., Bao, X., He, L., Lai, Y., Zu, L., Li, Y., and Su, S., 2016, "Tailpipe Emissions From Gasoline Direct Injection (GDI) and Port Fuel Injection (PFI) Vehicles at Both Low and High Ambient Temperatures," Environ. Pollut., **216**, pp. 223–234.

[9] Chan, T. W., Saffaripour, M., Liu, F., Hendren, J., Thomson, K. A., Kubsh, J., Brezny, R., and Rideout, G., 2016, "Characterization of Real-Time Particle Emissions From a Gasoline Direct Injection Vehicle Equipped With a Catalyzed Gasoline Particulate Filter During Filter Regeneration," Emiss. Control Sci. Technol., **2**(2), pp. 75–88.

[10] Boger, T., Rose, D., Nicolin, P., Gunasekaran, N., and Glasson, T., 2015, "Oxidation of Soot (Printex® u) in Particulate Filters Operated on Gasoline Engines," Emiss. Control Sci. Technol., **1**(1), pp. 49–63.

[11] Williams, J. L., 2001, "Monolith Structures, Materials, Properties and Uses," Catal. Today, **69**(1–4), pp. 3–9.

[12] Lambert, C. K., Chanko, T., Jagner, M., Hangas, J., Liu, X., Pakko, J., and Kamp, C. J., 2017, "Analysis of Ash in Low Mileage, Rapid Aged, and High Mileage Gasoline Exhaust Particle Filters," SAE Int. J. Engines, **10**(4), pp. 1595–1603.

[13] Konstantas, G., and Stamatelos, A., 2004, "Computer Aided Engineering of Diesel Filter Systems," Joint Meeting of the Italian and the Greek Section of the Combustion Institute, pp. 17–19.

[14] Thompson, G. J., Carder, D. K., Besch, M. C., Thiruvengadam, A., and Kappana, H., 2014, "In-Use Emissions Testing of Light-Duty Diesel Vehicles in the United States," Center for Alternative Fuels, Engines & Emissions, West Virginia University, Morgantown, WV, http://www. theicct.org/sites/default/files/publications/WVU_LDDV_in-use_ICCT_Report_Final_may2014.pdf

[15] Inoda, S., Nomura, Y., Ori, H., and Yabuzaki, Y., 2017, "Development of New Coating Technology Optimized for Each Function of Coated GPF," SAE Paper No. 2017-01-0929.

[16] Wang, Y., Wong, V., Sappok, A., and Munnis, S., 2013, "The Sensitivity of DPF Performance to the Spatial Distribution of Ash Inside DPF Inlet Channels," SAE Paper No. 2013-01-1584.

[17] Porter, Q., and Strzelec, A., 2019, "Benchtop Investigation of Filtration Efficiency and Pressure Drop Behavior of Commercial High Porosity Gasoline Particulate Filters," International Powertrains, Fuels and Lubricants Meeting, SAE Paper No. 2019-01-0054.

[18] Lambert, C. K., Bumbaroska, M., Dobson, D., Hangas, J., Pakko, J., and Tennison, P., 2016, "Analysis of High Mileage Gasoline Exhaust Particle Filters," SAE Int. J. Engines, **9**(2), pp. 1296–0941.

[19] Mikulic, I., Koelman, H., Majkowski, S., and Vosejpka, P., 2010, "A Study About Particle Filter Application on a State-of-the-Art Homogeneous Turbocharged 2 L DI Gasoline Engine," Aachener Kolloquium Fahrzeug- und Motorentechnik, Aachen, Germany.

[20] Korneev, S., and Onori, S., 2018, "Modeling the Transport Dynamics in Gasoline Particulate Filters," ASME Paper No. DSCC2018-9160.

[21] Oxarango, L., Schmitz, P., and Quintard, M., 2004, "Laminar Flow in Channels With Wall Suction or Injection: A New Model to Study Multi-Channel Filtration Systems," Chem. Eng. Sci., **59**(5), pp. 1039–1051.

[22] Nicolin, P., Rose, D., Kunath, F., and Boger, T., 2015, "Modeling of the Soot Oxidation in Gasoline Particulate Filters," SAE Int. J. Engines, **8**(3), pp. 1253–1260.

[23] Arunachalam, H., Pozzato, G., Hoffman, M. A., and Onori, S., 2017, "Modeling the Thermal Dynamics Inside a Ceria-Coated Gasoline Particulate Filter," First Annual IEEE Conference on Control Technology and Applications (CCTA 2017), Mauna Lani, HI, Aug. 27–30, pp. 99–105.

[24] Pozzato, G., Hoffman, M. A., and Onori, S., 2017, "Multi-Channel Physics-Based Modeling and Experimental Validation of an Uncoated Gasoline Particulate Filter in Clean Operating Conditions," American Control Conference (ACC), Seattle, WA, May 24–26, pp. 5392–5397.

[25] Gong, J., and Rutland, C. J., 2015, "PDF-Based Heterogeneous Multiscale Filtration Model," Environ. Sci. Technol., **49**(8), pp. 4963–4970.

[26] Gong, J., Viswanathan, S., Rothamer, D. A., Foster, D. E., and Rutland, C. J., 2017, "Dynamic Heterogeneous Multiscale Filtration Model: Probing Micro- and Macroscopic Filtration Characteristics of Gasoline Particulate Filters," Environ. Sci. Technol., **51**(19), pp. 11196–11204.

[27] Opitz, B., Drochner, A., Vogel, H., and Votsmeier, M., 2014, "An Experimental and Simulation Study on the Cold Start Behaviour of Particulate Filters With Wall Integrated Three Way Catalyst," Appl. Catal. B, **144**, pp. 203–215.

[28] Babu, M. K. G., Janakiraman, P. A., and Murthy, B. S., 1975, "Measurement of Exhaust Gas Velocity in an Internal Combustion Engine," SAE Trans., **84**, pp. 1675–1683.

[29] Ling, B., Tartakovsky, A. M., and Battiato, I., 2016, "Dispersion Controlled by Permeable Surfaces: Surface Properties and Scaling," J. Fluid Mech., **801**, pp. 13–42.

[30] Tartakovsky, A. M., Tartakovsky, D. M., Scheibe, T. D., and Meakin, P., 2008, "Hybrid Simulations of Reaction-Diffusion Systems in Porous Media," SIAM J. Sci. Comput., **30**(6), pp. 2799–2816.

[31] Korneev, S., and Battiato, I., 2016, "Sequential Homogenization of Reactive Transport in Polydisperse Porous Media," Multiscale Model. Simul., **14**(4), pp. 1301–1318.

[32] Auriault, J.-L., and Adler, P., 1995, "Taylor Dispersion in Porous Media: Analysis by Multiple Scale Expansions," Adv. Water Resour., **18**(4), pp. 217–226.

[33] Hou, T. Y., and Liang, D., 2008, "Multiscale Analysis for Convection Dominated Transport Equations," Discrete Contin. Dyn. Syst., **23**(1/2), pp. 281–298.

[34] CFD Direct, "OpenFOAM v7 User Guide," CFD Direct Ltd, Caversham, UK, accessed Feb. 18, 2020, http://cfd.direct/openfoam/user-guide/snappyhexmesh/

[35] Galindo, J., Serrano, J., Dolz, V., and Kleut, P., 2015, "Brayton Cycle for Internal Combustion Engine Exhaust Gas Waste Heat Recovery," Adv. Mech. Eng., **7**(6), p. 168781401559031.

[36] Mizushima, J., and Shiotani, Y., 2000, "Structural Instability of the Bifurcation Diagram for Two-Dimensional Flow in a Channel With a Sudden Expansion," J. Fluid Mech., **420**, pp. 131–145.

[37] Lei, T., 2011, *Statistics of Medical Imaging*, Chapman & Hall/CRC Interdisciplinary Statistics/CRC Press, Boca Raton, FL.

[38] Korneev, S. V., Yang, X., Zachara, J. M., Scheibe, T. D., and Battiato, I., 2018, "Downscaling-Based Segmentation for Unresolved Images of Highly Heterogeneous Granular Porous Samples," Water Resour. Res., **54**(4), pp. 2871–2890.